

MAGNETIC FIELD AND PLASMA SCALING LAWS: THEIR IMPLICATIONS FOR CORONAL HEATING MODELS

C. H. MANDRINI¹

Instituto de Astronomía y Física del Espacio, IAFE, CC. 67 Suc. 28, 1428 Buenos Aires, Argentina

P. DÉMOULIN

Observatoire de Paris, section Meudon, DASOP, URA 2080 (CNRS), F-92195 Meudon Principal Cedex, France

AND

J. A. KLIMCHUK

Naval Research Laboratory, Code 7675, Washington DC 20375-5352; mandrini@iafe.ub.ar

Received 1999 May 12; accepted 1999 September 30

ABSTRACT

In order to test different models of coronal heating, we have investigated how the magnetic field strength of coronal flux tubes depends on the end-to-end length of the tube. Using photospheric magnetograms from both observed and idealized active regions, we computed potential, linear force-free, and magnetostatic extrapolation models. For each model, we then determined the average coronal field strength, $\langle B \rangle$, in approximately 1000 individual flux tubes with regularly spaced footpoints. Scatter plots of $\langle B \rangle$ versus length, L , are characterized by a flat section for small L and a steeply declining section for large L . They are well described by a function of the form $\log \langle B \rangle = C_1 + C_2 \log L + C_3/2 \log (L^2 + S^2)$, where $C_2 \approx 0$, $-3 \leq C_3 \leq -1$, and $40 \leq S \leq 240$ Mm is related to the characteristic size of the active region. There is a tendency for the magnitude of C_3 to decrease as the magnetic complexity of the region increases. The average magnetic energy in a flux tube, $\langle B^2 \rangle$, exhibits a similar behavior, with only C_3 being significantly different. For flux tubes of intermediate length, $50 \leq L \leq 300$ Mm, corresponding to the soft X-ray loops in a study by Klimchuk & Porter (1995), we find a universal scaling law of the form $\langle B \rangle \propto L^\delta$, where $\delta = -0.88 \pm 0.3$. By combining this with the Klimchuk & Porter result that the heating rate scales as L^{-2} , we can test different models of coronal heating. We find that models involving the gradual stressing of the magnetic field, by slow footpoint motions, are in generally better agreement with the observational constraints than are wave heating models. We conclude, however, that the theoretical models must be more fully developed and the observational uncertainties must be reduced before any definitive statements about specific heating mechanisms can be made.

Subject headings: Sun: corona — Sun: magnetic fields — Sun: X-rays, gamma rays

1. INTRODUCTION

Ever since it was realized, some 60 years ago, that the solar corona is 2 orders of magnitude hotter than the underlying photosphere (Grottrian 1939), scientists have puzzled over the reason for these extreme conditions. What physical mechanism is responsible for heating the plasma to temperatures in excess of one million degrees? A number of plausible ideas have been proposed, including the dissipation of magnetohydrodynamic (MHD) waves (alternating current models) and the dissipation of stressed, current-carrying magnetic fields (direct current models). Unfortunately, the conversion of magnetic to thermal energy best occurs on spatial scales that are far smaller than can be observed directly by present-day solar instrumentation, and it has proven extremely difficult to identify the exact cause of the heating. We have been forced to rely on rather indirect means of determining the important processes involved.

One approach to the coronal heating problem is to investigate the height dependence of the heating rate (e.g., Sturrock, Wheatland, & Acton 1996; Kano & Tsuneta 1996; Priest et al. 1998). Some models predict preferential heating at higher or lower altitudes in the corona, while others

predict a more uniform distribution. Another promising approach is to determine how the heating rate correlates with observable physical parameters. Scaling laws can be derived both from observations and theory, and the results can be compared to evaluate the models. For example, many models predict that the heating rate has a power-law dependence on both the strength of the magnetic field and the length of the field lines. Because the dependence is different for each model, the observed correlations provide a valuable test.

Golub et al. (1980) and more recently Falconer (1997) and Fisher et al. (1998) have examined scaling relationships for entire active regions. They compared measures of the total heating in active regions with various “global” magnetic quantities. Fisher et al. found that the 1–300 Å X-ray luminosity of an active region scales nearly linearly with its total unsigned magnetic flux. In addition, they found no significant correlation between the X-ray luminosity and the total unsigned vertical electric current (other than what can be accounted for by the correlation between flux and current). The authors concluded that coronal heating bears no direct relationship to *large-scale* currents that are detectable by ground-based vector magnetographs.

This may seem surprising, given that the magnetic free energy available for plasma heating is directly related to the currents that are present in the stressed magnetic fields. However, it has been known since the time of *Skylab* that

¹ Member of the Carrera del Investigador Científico, CONICET, Argentina.

most of the hot emission from the corona originates in thin loop structures that occupy only a very small fraction of the coronal volume (e.g., Orall 1981; Bray et al. 1991). Acton (1996) attributes 23% of the X-ray luminosity from active regions to 4% of the active region area, and therefore 1% of active region volume. The result of Fisher et al. (1998) is therefore not totally unexpected; the currents involved in coronal heating apparently have a much smaller scale than those revealed by the Mees Stokes Polarimeter data used in their analysis (see also Metcalf et al. 1994). It is nonetheless interesting that the small-scale currents associated with loop heating are not more closely related to the large-scale current systems responsible for shear and twist patterns observed in collections of loops (e.g., Rust & Kumar 1996; Schmieder et al. 1996; Pevtsov, Canfield, & McClymont 1997).

Recognizing that coronal loops are the fundamental building blocks of the corona, Klimchuk & Porter (1995) attacked the coronal heating problem by determining scaling laws for a sample of 47 loops observed by the Soft X-Ray Telescope (SXT) aboard *Yohkoh* (see also Porter & Klimchuk 1995). They found that loop temperature and length are statistically uncorrelated and that pressure varies inversely with length to approximately the first power. Noting that the observed lifetimes of the loops are much longer than their cooling times, the authors then used quasi-static loop equilibrium theory to infer that the volumetric heating rate scales inversely with length to approximately the second power.

This is a very powerful result, since different coronal heating models make different predictions about what the scaling between heating rate and length should be. Klimchuk & Porter were unable to make definitive tests, however, because the model predictions depend upon the statistical relationship that exists between field strength and loop length, and this relationship was unknown at the time of their study. To make progress, they assumed a power-law dependence of the form

$$B \propto L^{\delta}, \quad (1)$$

where B is the field strength and L is the length of the loop. They then showed that three coronal heating models involving braided fields, twisted fields, and resonantly absorbed Alfvén waves are consistent with the SXT observations only if $\delta = -0.5, 0$, and -2 , respectively. It was unknown which, if any, of these values is correct, or even whether the single power-law form of equation (1) is appropriate. A comparison with *Skylab* results relating the average pressures and field strengths of entire active regions (Golub et al. 1980) suggested that $\delta \approx -0.7$, thereby favoring the braided field model (Parker 1983, 1988), but no firm conclusions could be drawn.

The general goal of our work reported here is to explore the statistical relationship between the field strength and length of coronal magnetic flux tubes. Surely, B tends to decrease with L , but what is the nature of the relationship, and how does it depend upon the size and complexity of the active region? A more specific goal is to evaluate whether the power-law form assumed by Klimchuk & Porter is reasonable and, if so, to determine the value of δ . Only then can coronal heating models be rigorously constrained.

Our basic approach is to construct potential, linear force-free, and magnetostatic models of active regions and to generate scatter plots of field strength versus length for the

flux tubes which comprise the regions. We then characterize the $B(L)$ relationship by fitting the scatter plot data to well-chosen functions. We consider both observed active regions, including many from the Klimchuk & Porter study, and idealized active regions, which allow us to more easily investigate the factors which control the $B(L)$ relationship (shear, complexity, etc.).

Our paper is laid out as follows. In § 2, we describe the observations, model construction, and computation of magnetic flux tube variables. In § 3, we present the scatter plots and functional fits, and we propose a general function that represents the data quite accurately over all values of L . We then consider in § 4 a restricted range of L corresponding to the *Yohkoh* loops studied by Klimchuk & Porter. We show that a single power law is, indeed, appropriate for this range. In § 5, we use our results to constrain models of coronal heating, including, but not limited to, the three models considered by Klimchuk & Porter. Finally, we summarize and conclude in § 6.

2. METHOD OF ANALYSIS

2.1. Description of the Data

Because we wish to combine our results with those of Klimchuk & Porter (1995), we decided to examine many of the same active regions (ARs) used in their study. We selected seven regions based on the availability of magnetograms and the desire to have observations close to disk center (see Table 1, first group of ARs). About one-quarter of the loops in the Klimchuk & Porter sample are contained in these regions. All but one lie within 30° of disk center, the exception being located at S26 W35. Only longitudinal magnetograms are available for these regions, so we must rely on potential field models of the coronal field. The proximity of the regions to disk center allows us to extrapolate from the observed line-of-sight fields without making significant adjustments for geometrical effects, a procedure which can sometimes introduce errors. As discussed in § 2.3, we have compared the modeled field lines to observed soft X-ray loops to verify that the models are reasonable.

The active regions in this group are fairly typical and represent a variety of types, ranging from young and well-formed to old and decayed. None were flaring at the time of the *Yohkoh* observations, and the loops appeared to be in quasi-static equilibrium. To extend our study, we also considered a second set of seven regions that are different in the sense that they were observed flaring close to the time of the magnetic field observations (see Table 1, second group of ARs). Their magnetic field topology and its relationship to coronal events such as solar flares or X-ray bright points (XBPs) have been analyzed in several papers in order to determine the most likely mechanism for energy release (see Mandrini et al. 1996; Schmieder et al. 1996; Démoulin et al. 1997; and references therein). These ARs are also located close to disk center and they are mature regions, except the one in which an XBP was observed (AR 7493), which is old and decayed. Their configurations range from bipolar to quadrupolar, some including several parasitic polarities, with different degrees of magnetic shear.

The coronal magnetic field is computed from the longitudinal field component obtained at five different observatories, depending on the studied AR, as indicated in Table 1. We have also included in this table the NOAA AR number and the magnetogram observation date. In the case of the

TABLE 1
LIST OF THE ARs INCLUDED IN THE STUDY

Number	AR (NOAA)	Date	Observatory	α_s (Mm ⁻¹)
1	7056	1992 Feb 14	KPNO	0.
2	7117	1992 Mar 30	KPNO	0.
3	7222	1992 Jul 14	KPNO	0.
4	6982	1991 Dec 26	KPNO	0.
5	7135	1992 Apr 22	KPNO	0.
6	7183?	1992 Jun 5	KPNO (see text)	0.
7	7064	1992 Feb 20	KPNO	0.
8	2511	1980 Jun 13	PO and MSFC	0.
9	2511	1980 Jun 15	PO and MSFC	-0.006
10	2776	1980 Nov 5	MSFC	-0.025
11	7493	1993 May 1	MSO and ESO	0.02
12	2372	1980 Apr 6	MSFC	0.
13	2779	1980 Nov 12	MSFC	-0.019
14	6718	1991 Jul 11	KPNO	0.013

region observed on 1992 June 5 no AR is identified in Solar Geophysical Data (SGD) records at the location of SXT loops on that date, but we believe that the observed field corresponds to the decaying state of AR 7183 (SGD 576, Part 1). The magnetograph of Kitt Peak National Observatory (KPNO) has been described by Livingston et al. (1976). It provides daily full disk longitudinal magnetic field maps with a spatial resolution of around 1". The vector magnetograms from Mees Solar Observatory (MSO), Hawaii, have been obtained with the Stokes Polarimeter (Mickey 1985) with a resolution of 2".8. The vector magnetographs from the Marshall Space Flight Center (MSFC) in Huntsville (Hagyard et al. 1982) and the Einsteinurm Solar Observatory (ESO) in Potsdam (Staude, Hofmann, & Bachmann 1991) have a spatial resolution of 2".5 and 3", respectively. Finally, the longitudinal magnetograph at Paris Observatory (PO) in Meudon has a spatial resolution of 1".2 × 2" (Rayrole 1980).

2.2. Magnetic Field Modeling

The magnetic field is not measured accurately in the corona and therefore it must be computed from photospheric magnetograms. This so-called extrapolation method is based on certain physical laws. Because the plasma velocity is usually much lower than the Alfvén speed, we use the following magnetohydrostatic equations:

$$\frac{1}{\mu_0} (\nabla \times \mathbf{B}) \times \mathbf{B} - \nabla p - \rho \mathbf{g} = 0, \quad (2)$$

$$\nabla \cdot \mathbf{B} = 0. \quad (3)$$

Low (1992) has found solutions to these equations by writing the current density ($\mathbf{j} = \nabla \times \mathbf{B}/\mu_0$) in terms of Euler potentials. The solutions which are linear in \mathbf{B} are of great interest because they can be used with any boundary conditions, in particular those provided by magnetograms (while the few known analytical nonlinear solutions are restricted to boundary conditions which do not represent active regions and, moreover, have a trivial magnetic topology). We consider a Cartesian system of coordinates, where z refers to the height above the photosphere, located at $z = 0$. For any given function of height, $F(z)$, Low found a class of solutions satisfying the following simplified equation:

$$\nabla \times \mathbf{B} = \alpha_s \mathbf{B} + F(z) \nabla B_z \times \mathbf{u}_z, \quad (4)$$

where \mathbf{u}_z is the vertical unit vector, and α_s is a constant. With $F(z) = 0$, we have the usual linear force-free field solutions including the potential solution for $\alpha_s = 0$.

The function $F(z)$ is related to the plasma pressure by

$$p = p_0(z) - F(z) \frac{B_z^2}{2\mu_0}, \quad (5)$$

where $p_0(z)$ is the plasma pressure of the hydrostatic atmosphere without magnetic field. In order to estimate simply the effects of the plasma, we suppose an atmosphere in which the finite Lorentz force decreases with height in such a way that

$$F(z) = a \exp(-z/H). \quad (6)$$

We further suppose that H is comparable to the plasma pressure scale height. For consistency, the hydrostatic pressure $p_0(z)$ can also be taken of this form, but it is worth noting that $p_0(z)$ has no influence on the magnetic field and so on the results reported below.

Solutions of equation (4) are found by means of Fourier transforms in the horizontal directions (x, y), leading to an ordinary differential equation in the vertical direction for each Fourier mode of B_z . The components B_x , B_y , the plasma pressure p , and density ρ are then computed from the B_z solution and equations (2) and (3). The practical implementation of the problem is identical to the linear force-free field case (see Démoulin et al. 1997, for the use of the fast Fourier transform and also for the transformation of coordinates for regions located away from disk center).

2.3. Characteristics of the Computed Magnetic Configurations

We have computed three types of coronal magnetic field models: potential, linear force free, and magnetostatic. Since only longitudinal magnetograms are available for the first group of observed active regions, we used potential fields ($\alpha_s = 0$) to model them. We find that these models are in generally good agreement with the *Yohkoh* observations. This is demonstrated in Figure 1, where the soft X-ray loop indicated by the arrow is seen to have a similar shape to the extrapolated field lines. Local agreement can usually be improved by choosing a nonzero value of α_s , but this often results in greater discrepancies elsewhere in the active region. It is our experience that *Yohkoh* images are not

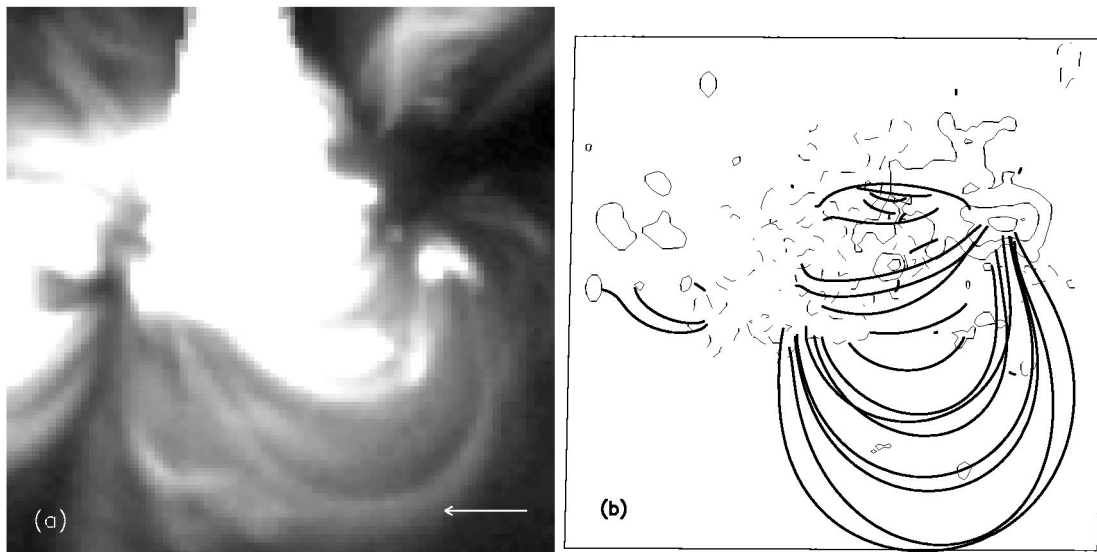


FIG. 1.—Comparison of (a) the observed soft X-rays loops with (b) the coronal field lines computed for a potential model of the photospheric field of AR 7135. The arrow in (a) points to the loop included in Klimchuk & Porter (1995) study. (b) is a three-dimensional view of the AR in the observer's perspective. Three isocontour levels of B_t ($\pm 100, 500, 1000$ G) are shown with positive and negative values drawn with solid and dashed lines, respectively. The size of the region in both figures is 240×240 Mm. North is up, and west is to the right.

sufficient for determining the nonzero α_s that best characterizes the entire active region. Furthermore, we believe that the potential field approximation is adequate for our purposes here.

For the second group of active regions, we have both vector magnetograms and $H\alpha$ images to constrain the models and, therefore, we could more easily construct linear force-free fields. The parameter α_s was determined by fitting the direction of either the observed transverse field component or the $H\alpha$ fibrils in the surroundings of the flare brightenings. The resulting values are given in Table 1.

In § 3.2, we consider idealized active regions produced by magnetic point charges buried below the photosphere. One motivation is to investigate the effects that the coronal plasma may have on the field. How does it distort the field lines and influence the relationship between B and L ? To address this issue, we constructed a series of magnetostatic models [$F(z) \neq 0$] corresponding to different values of a in equation (6). As we show later, the effects of the plasma pressure and gravity forces are minimal in the low- β coronal environment.

2.4. Definition of Averages of the Magnetic Field

The magnetic flux tubes which comprise these different models tend to expand with height, and so the field strength is a function of position along the tube. In contrast, most coronal heating models are worked out in idealized configurations in which the field is both nearly uniform and straight. Furthermore, flux tubes that correspond to distinguishable X-ray loops are observed to have nearly constant cross sections (Klimchuk et al. 1992). In order to link our analysis to the heating models and to the Klimchuk & Porter results, it is necessary that we define certain flux tube-averaged magnetic quantities.

We first consider the average of the field strength B over the tube volume:

$$\langle B \rangle = \frac{\int B dV}{\int dV} \approx \frac{L}{\int ds/B}, \quad (7)$$

where dV is the elemental volume, s is the curvilinear coordinate along the central axis of the tube, and $L = \int ds$ is its length. We are able to replace the volume integral by a line integral under the assumption that the tube is thin (negligible variation of B within the cross section), where we have made use of magnetic-flux conservation (eq. [3]).

Because most coronal heating models depend on a power of B that ranges between 1 and 2, we also consider the average of B^2 , the magnetic energy density:

$$\langle B^2 \rangle = \frac{\int B^2 dV}{\int dV} \approx \frac{\int B ds}{\int ds/B}. \quad (8)$$

In both cases, the volume average tends to preferentially weight the top of the loop, where the cross section is larger. On the other hand, the nonlinear nature of B^2 gives emphasis to the feet, where the field is stronger.

3. A LAW FOR THE CORONAL MAGNETIC FIELD

For each of our magnetic field models, we determine $\langle B \rangle$, $\langle B^2 \rangle$, and L for a subset of field lines (infinitesimally thin flux tubes) that have footpoints regularly spaced on the photosphere. This is accomplished by tracing the field lines from a rectangular grid of footpoint starting positions. The grid spacing is typically 1 Mm, and the number of traced field lines is of order 10^4 . Note that the ends of the traces occur at conjugate footpoint positions that are not necessarily evenly spaced.

We then generate scatter plots of $\langle B \rangle$ versus L and $\langle B^2 \rangle$ versus L using only the field lines that satisfy certain selection criteria. Because we are interested in coronal loops and coronal heating, we limit our analysis to field lines for which (unless noted differently): the length is in the interval [1, 1000] Mm, the average coronal field strength is above 1 G, and the photospheric field strength of both loop feet, B_f , is above 10 G.

Typically 500 to 2×10^3 field lines satisfy these criteria in each model. Our reasons for adopting the criteria are twofold: first, 10 G is the typical noise level of the magneto-

grams, and we wish to exclude noisy data; and second, weak field regions are not expected to contribute significantly to coronal heating, and including them in the scatter plots would produce an unwanted bias in the statistical relationship we are trying to establish. It is worth noting that B_f is the average magnetic flux measured in a magnetogram with finite spatial resolution. If photospheric magnetic flux is concentrated in unresolved flux tubes with a field strength of ≈ 1500 G, as generally believed, then $B_f \geq 10$ G implies a magnetic filling factor greater than 1%.

Sams, Golub, & Weiss (1992) and Schmieder et al. (1996) have shown that X-ray coronal loops are observed mainly in regions of intermediate photospheric field strength (see also Aschwanden et al. 1999), and since we are especially interested in the flux tubes that correspond to such loops, we also consider the more restrictive interval $100 \leq B_f \leq 500$ G. In some cases, the number of traced field lines satisfying this criterion is not statistically significant, and we do not include those results.

3.1. Observed Active Regions

Figure 2 shows scatter plots of $\langle B \rangle$ and $\langle B^2 \rangle$ versus L for region number 6 in Table 1. Figures 2a and 2b correspond to field lines with $B_f \geq 10$ G, while Figures 2c and 2d correspond to field lines with $100 \leq B_f \leq 500$ G. In each case, the distribution of points has a distinctive shape characterized by a nearly flat section for small L and a steeply declin-

ing section for large L . The transition between the two sections occurs fairly abruptly at a noticeable knee in the distribution. A large dispersion is seen in Figures 2a and 2b for field lines shorter than ≈ 30 Mm. This is due to the presence of numerous small flux concentrations in this particular active region. Since the region is in its decaying state and the flux concentrations are weak, few field lines have $100 \leq B_f \leq 500$ G as shown in Figures 2c and 2d.

The trend evident in Figure 2 is present for all the ARs included in Table 1. Differences in the individual distributions are related to the unique magnetic characteristics of each case; that is, the number, intensity, and relative positions of the photospheric flux concentrations. In particular, the location of the distribution knee (i.e., the value of L at which the distribution changes slope) is related to a typical AR length scale, as we discuss further below. Based on the universal shape of the distributions, we propose that $\log \langle B \rangle$ and $\log \langle B^2 \rangle$ have a functional dependence on L with the following general form:

$$F_1(L) = C_1 + C_2 \log L + \frac{C_3}{2} \log (L^2 + S^2). \quad (9)$$

The four parameters C_1 , C_2 , C_3 , and S are unique for each active region. We determine their values by performing least-squares fits to the scatter plot data. The fits for region number 6 are shown as continuous curves in Figure 2. In practice, we find that only C_3 and S differ significantly from

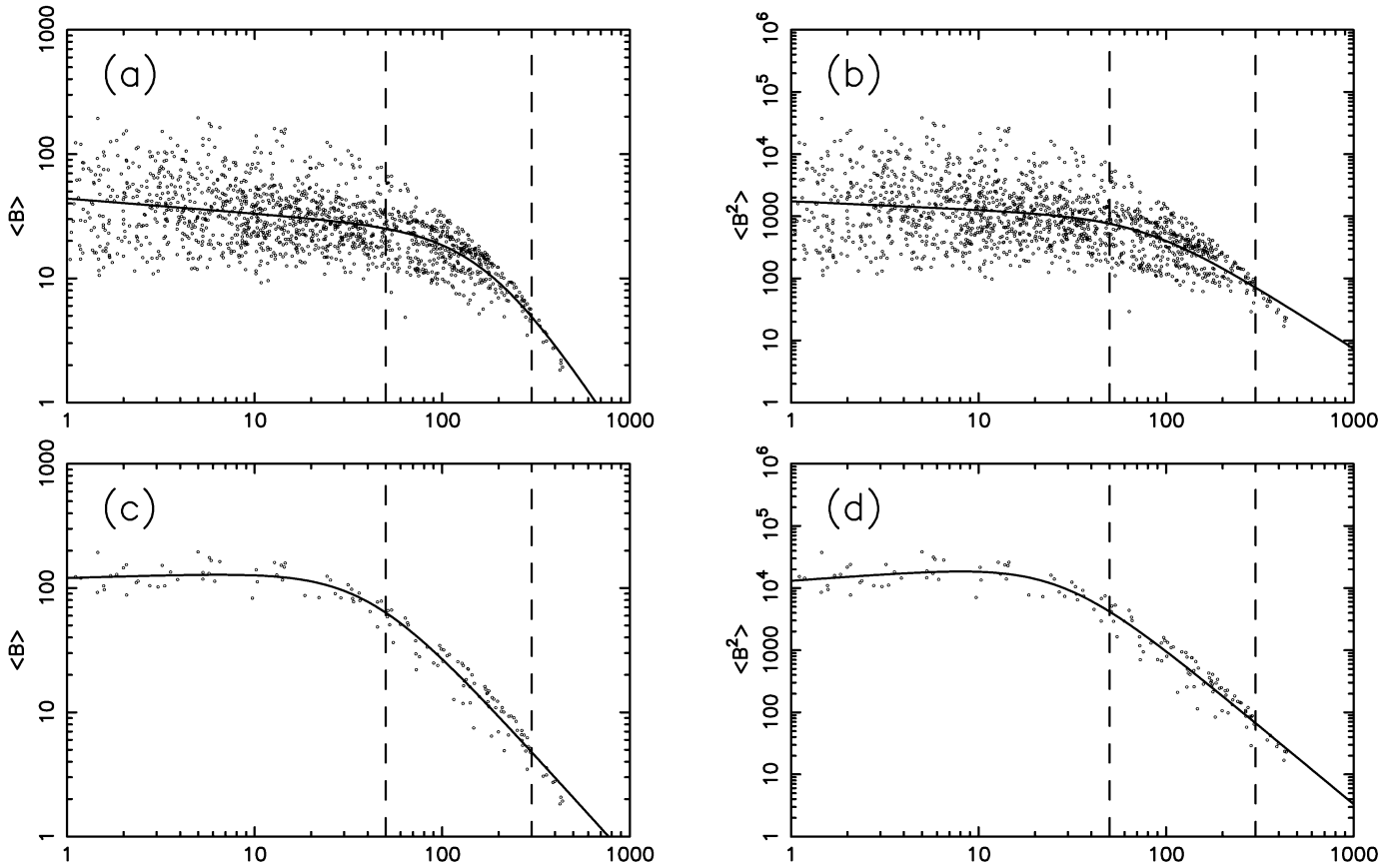


FIG. 2.—Scatter plots of $\langle B \rangle$ and $\langle B^2 \rangle$ vs. L for region number 6 in Table 1. The axes have logarithmic scales with the field line length L (abscissa) measured in Mm and the magnetic field B in G. Each point represents a computed field line. (a) and (c) correspond to $\langle B \rangle$, while (b) and (d) correspond to $\langle B^2 \rangle$ (as defined in § 2.4). (a) and (b) are for field lines for which $B_f > 10$ G at both photospheric feet. (c) and (d) are the results for a restricted set of field lines with $100 < B_f < 500$ G. The curve in each plot is a least-squares fit of function $F_1(L)$ to the points, and the two vertical dashed lines indicate the interval of coronal loop lengths in the study of Klimchuk & Porter (1995).

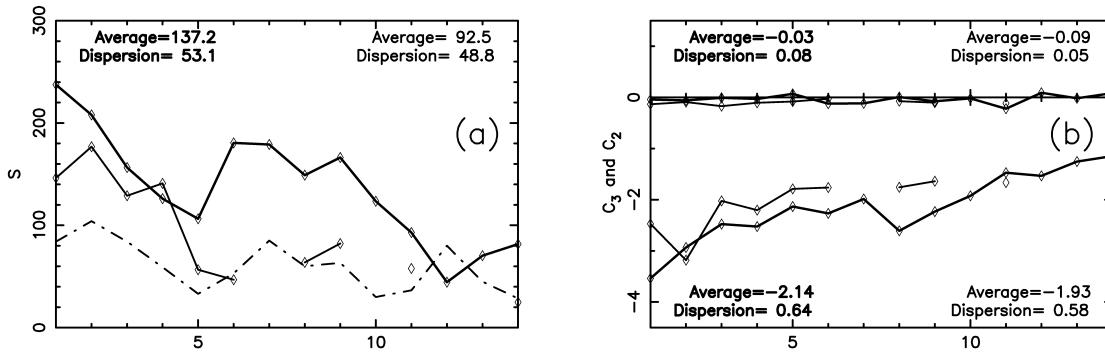


FIG. 3.—Results from fitting function F_1 to the $\langle B \rangle$ vs. L scatter plot data derived from the observed active regions (Fig. 2 being one example). The numbers in the abscissa are those given in the first column of Table 1. Parameter S is plotted in (a), and coefficients C_2 (top) and C_3 (bottom) are plotted in (b). The thick (thin) lines are for $B_f \geq 10$ G ($100 < B_f < 500$ G). The dash-dotted line in (a) represents the estimated active region size S_{AR} as given by eq. (10).

one region to the next; C_2 is nearly the same for all regions, and C_1 is not relevant to our purposes here.

When $F_1 = \log \langle B \rangle$, equation (9) simplifies to the power law $\langle B \rangle \propto L^\delta$ in the two limits $L \ll S$ and $L \gg S$, where $\delta = C_2$ and $\delta = C_2 + C_3$, respectively. For L much larger than the size of ARs (typically 100 Mm), the dipolar term dominates over the other multipolar terms of the magnetic field expansion. In this limit, we expect that $\delta = C_2 + C_3 = -3$. The extrapolation models show exactly this behavior for field lines longer than 1000 Mm. These field lines are, however, far longer than the observed soft X-ray loops seen in ARs (and considered by Klimchuk & Porter). This suggests that the slope δ should have a magnitude less than 3 if we restrict the range of lengths to those of observed coronal loops. As can be seen in Figure 2, we have effectively limited our analysis to field lines shorter than ≈ 500 Mm by requiring that $\langle B \rangle$ be greater than 1 G.

Figure 3 shows the parameters S , C_2 , and C_3 obtained from fits to the $\langle B \rangle$ versus L scatter plot data for the different active regions, plotted as a function of region number from Table 1. Thick solid lines connect the values obtained with the criterion $B_f \geq 10$ G, and thin solid lines connect the values obtained with the criterion $100 \leq B_f \leq 500$ G. Regions 7, 10, 12, and 13 do not have enough traced field lines satisfying the latter criterion to be included. As described above, the regions have been divided into two groups: those belonging to the Klimchuk & Porter study and those that have undergone recent flaring activity. Within each group, the regions are ordered according to their magnetic complexity, beginning with relatively simple configurations and progressing to more complex ones. Thus, in the first group we put first the well-developed ARs

(with several strong spots), then the less intense ones, and finally the “old” and decayed ARs. The ordering in the second group follows a similar trend. The first AR is basically bipolar, and afterward the number of polarity centers, together with the complexity of their distribution, increases. The quality of the least-squares fits is indicated by the Pearson’s correlation factor r . Its average is given in Table 2 for all 14 active regions combined.

We see from Figure 3 that C_2 hovers very close to 0 in all cases, indicating that average field strength is nearly independent of length for $L \leq S$. C_3 ranges mostly between -3 and -1 and tends to be less negative for more complex regions. Its average value is ≈ -2 for both of the B_f criteria. The parameter S varies from about 40 to 240 Mm, and we expect that it is related to some typical AR length scale. To verify this, we have computed a quantity called the AR size, S_{AR} , which is the flux-weighted mean distance between opposite polarity photospheric fields. It is defined as

$$S_{AR}^2 = (X_p - X_n)^2 + (Y_p - Y_n)^2, \quad (10)$$

where

$$X_p = \frac{\sum x B_z}{\sum B_z}, \quad Y_p = \frac{\sum y B_z}{\sum B_z} \quad (11)$$

give the mean position of the positive concentrations ($B_z > 0$), and similar expressions give the mean position of the negative concentrations ($B_z < 0$). Only vertical field strengths $|B_z| > 10$ G are included to avoid noisy data. The computed values of S_{AR} are connected with a dash-dotted line in Figure 3a. As anticipated, there is a reasonably good correlation with S .

TABLE 2
AVERAGE VALUES OF C_3 AND CORRELATION FACTORS TO F_1

B_f Range	$C_3(\langle B \rangle)$	$C_3(\langle B^2 \rangle)$	$r(\langle B \rangle)$	$r(\langle B^2 \rangle)$
Observed Regions				
$10 \leq B_f$	-2.14 ± 0.64	-2.81 ± 0.69	0.67 ± 0.16	0.56 ± 0.20
$100 \leq B_f \leq 500$ G	-1.93 ± 0.58	-2.57 ± 0.65	0.91 ± 0.06	0.88 ± 0.07
Models				
$10 \leq B_f$	-1.71 ± 0.55	-2.5 ± 0.74	0.75 ± 0.07	0.65 ± 0.07
$100 \leq B_f \leq 500$ G	-2.00 ± 0.40	-2.92 ± 0.56	0.94 ± 0.05	0.91 ± 0.06

The results obtained for $\langle B^2 \rangle$ are similar to those obtained for $\langle B \rangle$: a very flat distribution for $L \ll S$ ($C_2 \approx 0$.) and a steeply declining section for large L . The main difference is that the coefficient C_3 is more negative (see Table 2). The coefficient C_3 obtained with $\langle B^2 \rangle$ is not twice as large as the one obtained with $\langle B \rangle$ (as one may have expected) because of the following reason. For long field lines the numerator of equation (8), $\int B ds$, is mainly dominated by the part which is close to the photosphere, then it is nearly independent of the length L , while the numerator of equation (7) is simply L . From this consideration one rather expects that $C_3(\langle B^2 \rangle) \approx C_3(\langle B \rangle) - 1$. The computations show slightly closer values: $C_3(\langle B^2 \rangle) \approx C_3(\langle B \rangle) - 0.65$ (see Table 2).

3.2. Simplified Configurations

In order to gain insight into the dependence of the proposed law, $F_1(L)$, on the properties of the magnetic configuration, we have constructed a series of idealized theoretical models of varying complexity. The models are based on subphotospheric magnetic charges of differing strength and position. Figure 4 shows an example produced by six charges corresponding to three bipoles. The models are used to derive theoretical magnetograms, which are then extrapolated into the corona in the same way as the observed magnetograms. In the case of potential and linear-force models, the coronal magnetic field can also be derived analytically. A comparison between the two fields shows the distortions introduced by the extrapolation procedure. These distortions are caused by the finite size and resolution of the theoretical magnetograms, as well as by the periodicity imposed by the fast Fourier transform. All the theoretical magnetograms presented here have a size of 500×500 Mm and resolution of 2 Mm, but other values appropriate to different magnetographs have also been tried. In all cases,

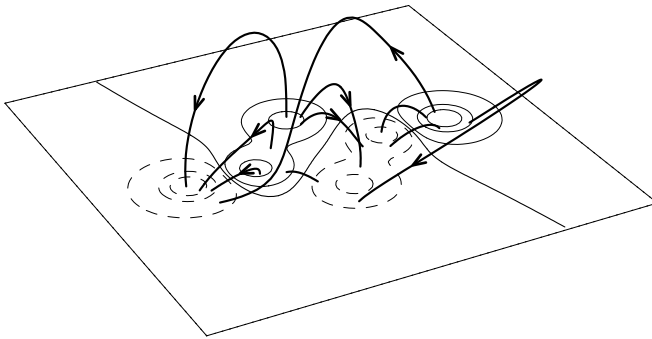


FIG. 4.—Example of one simplified magnetic configuration (number 16 and 21 in Table 3). The isocontour values of the field are the same as in Fig. 1. Several field lines have been added.

we verify that the extrapolation procedure has a negligible effect on the results.

The idealized models are separated into several groups, each of which highlights a particular property of the field. The defining characteristics are listed in Table 3 and discussed below. For each model, we generate scatter plot data using the same L , $\langle B \rangle$, and B_f selection criteria as before. Least-squares fits are performed, and the resulting fit parameters are plotted in Figure 5. Once again, only the $\langle B \rangle$ results are given because the $\langle B^2 \rangle$ results are so similar (see Table 2).

The simplest model (number 1) is built from two magnetic charges of opposite sign separated by $D = 120$ Mm and located a depth $d = 10$ Mm below the photosphere. The magnitudes of the charges are chosen to produce a maximum vertical field strength of 2000 G in the photosphere. The potential field associated with this model is the simplest approximation of an active region. It has a $B(L)$ relationship that can be simply understood by analyzing the general dependence of the formula for two monopoles separated by D :

$$B \propto [(z + d)^2 + (D/2)^2]^{-3/2} \propto (L^2 + D^2)^{-3/2}. \quad (12)$$

So for the full range of lengths, the expected values are $C_2 = 0$ and $C_3 = -3$. For the restricted range of lengths considered here, the scatter plot fits give $C_2 \approx 0.1$ and C_3 between -2.1 and -2.7 (see Fig. 5); this implies that the slope for $L > S$ is slightly less steep than the dipole limit at large loop lengths (-3).

The following polarity fields of active regions are usually much more dispersed than the preceding polarity fields. We investigate the effect of this asymmetry by placing the following polarity charge at progressively greater depths below the photosphere. The resulting configurations are characterized by an asymmetry parameter A_s (see Table 3), defined to be the ratio between the depth of the following polarity charge to the depth of the preceding polarity charge. As A_s becomes larger (models 1–5), the scale of the active region grows, and there is a corresponding increase in the fit parameter S (Fig. 5a). In addition, greater asymmetry causes a sharper decrease in $\langle B \rangle$ for $L > S$, giving a more negative coefficient C_3 .

Many ARs have one or more parasitic bipoles embedded within the primary bipolar structure. Such configurations have a complex topology that is typical of flaring ARs (see Démoulin et al. 1997 and references therein). To simulate this, we add a second bipole at the center of the main one, with half of its size and strength. Models 6–14 demonstrate the effect of increasing the angle between the bipoles, ϕ_2 , from 0 to π in the horizontal plane. At $\phi_2 = \pi$, the bipoles are antiparallel and the configuration is that of a quad-

TABLE 3
PARAMETERS FOR THE THEORETICAL CONFIGURATIONS

Configuration N^0	N^0 of Bipoles	A_s	ϕ_2	ϕ_3	α_s (Mm^{-1})	a
1–5	1	1–3.			0.	0.
6–14	2	1.	$0-\pi$		0.	0.
15	3	1.	0	$\pi/2$	0.	0.
16–20	3	1.	π	$\pi/2$	0.2×10^{-2}	0.
21–24	3	1.	π	$\pi/2$	0.	0., 0.2, 0.5, 1.

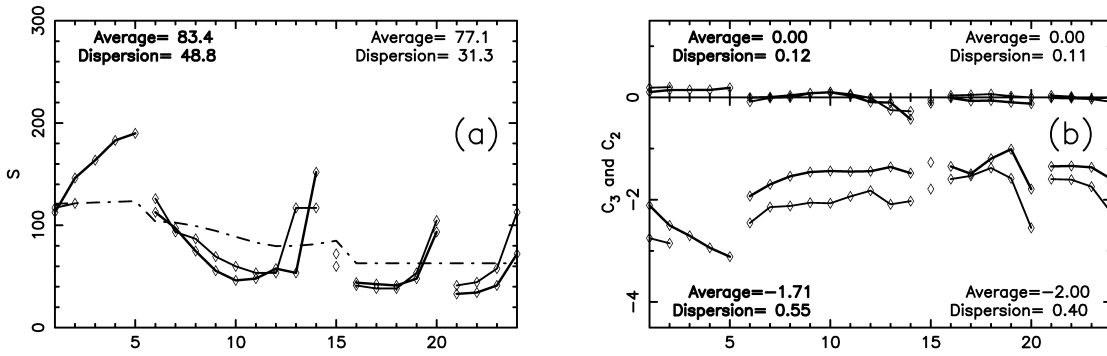


FIG. 5.—Results from fitting function F_1 to the $\langle B \rangle$ vs. L scatter plot data derived from the idealized theoretical models. The format is identical to that of Fig. 3, and the model numbers in the abscissa are those given in the first column of Table 3. Models 1–5 correspond to a single bipole with increasing asymmetry in the areas of the preceding and following polarities. Models 6–14 correspond to two bipoles with increasing angular deviation, from parallel to antiparallel. Models 15–24 correspond to three bipoles with increasing shear (16–20) and increasing plasma pressure (21–24).

rupole. In comparing models 1 and 6–14, we see a general tendency for C_3 to become less negative as the complexity of the field increases (Fig. 5), although the behavior is not perfectly monotonic. This trend continues as we further increase the complexity by adding a third bipole of the same size and strength as the second, but at an angle $\phi_3 = \pi/2$ (models 15 and 16, where $\phi_2 = 0$ and π , respectively). In all cases, C_2 remains close to zero, indicating once again that the average field strength is nearly independent of the length for $L \leq S$.

It may seem counter intuitive that $\langle B \rangle$ decreases less rapidly with L as new bipoles are added and the complexity of the field increases. Greater complexity implies that higher order multipoles are more important, and such multipoles decrease more rapidly with distance from the current source. The apparent discrepancy has two causes. First, there is a nontrivial relation between the length of a field line and its mean distance from the origin in the multipolar expansion. Second, most of the field lines included in our scatter plots reside close enough to the origin that the angular dependence of the multipoles is very important. It is only at large distances and when the topology is trivial that simple conclusions can be drawn. The results are explained by the following consideration. As the magnetogram complexity increases, as does the magnetic topology, the field lines become shorter, except for the ones with a length larger than the active region size. This implies a larger number of short field lines with a stronger average field. The shortening of the field lines in the vicinity of the curve knee dominates and the coefficient C_3 becomes less negative in this case.

To investigate the effect of magnetic shear, we take the case of three bipoles ($\phi_2 = \pi$, $\phi_3 = \pi/2$) and vary the parameter α_s in equation (4) from 0.0 to 0.02 Mm^{-1} (models 16–20). We have also done this for the single bipole configuration and find similar results. Except for the last models in the series, which have unphysical properties discussed below, the general trend is for S to remain constant and C_3 to become less negative as the field becomes progressively sheared. The reasons for this behavior can be understood as follows. Increasing α_s corresponds to rotating the field. The mean separation of the opposite polarity poles, S_{AR} , is not affected (dash-dotted line in Fig. 5), and this is the dominant factor in determining the value of S . Concerning C_3 , it is a well-known property of magnetic configurations that they inflate (i.e., expand outward) whenever the field is sheared

(e.g., Klimchuk 1990). For linear force-free fields, the shear is greatest in the outer parts of the active region, away from the neutral line. Longer field lines are lengthened more than shorter ones, and the net effect is to decrease the slope of $\langle B \rangle$ versus L . The opposite is true of nonlinear force-free fields for which shorter field lines near the neutral line have the greatest shear. This is more typical of observed active regions (e.g., Schmieder et al. 1996). We conclude that the influence of magnetic shear can be significant and that it depends on the detailed distribution of the shear and associated electric currents. Such information is not usually available in observed ARs, in particular when the measured transverse field strength is below a few hundred G and the currents are difficult to infer. It is for this reason that we restrict the deduction of F_1 to low-shear regions.

These general trends break down when α_s exceeds a critical level related to the horizontal size of the computational box S_b : $\alpha_{crit} = 2\pi/S_b \approx 1.2 \times 10^{-2} \text{ Mm}^{-1}$ for the value $S_b = 500 \text{ Mm}$ used here. Beyond this, the first harmonics of the solutions oscillate with height and have substantial amplitude. They have infinite energy and are discarded in the computations (see Démoulin et al. 1997). This explains the nonmonotonic change in the variation of S and C_3 at the end of the shear sequence (models 16–20) in Figure 5.

The final effect that we consider is that of a finite β coronal plasma. We compute magnetohydrostatic solutions to equation (4) using a typical pressure scale height $H = 100 \text{ Mm}$ (see eq. [6]), although changing H by a factor 2 has little effect on the fit parameters. In the present model, there is a plasma pressure depletion $[\delta p = a(B^2/2\mu_0) \exp(-z/H)]$ where the field is strong and nearly vertical ($B_z \approx B$) when a is positive. This is consistent with measurements of the pressure above strong fields, such as sunspots. Because the plasma pressure should be positive, $p_0(z)$ should be at least as large as δp (for the same height z). This implies a plasma pressure greater than $a(B^2/2\mu_0) \exp(-z/H)$, where the magnetic field is horizontal. The β there is as large as $a \exp(-z/H)(B/B_h)^2$ (where B_h and B are, respectively, the field strength at which the field is horizontal and vertical at the same height z). Typical β values in the quiet corona are in the range $[10^{-4}, 10^{-3}]$, which implies a values approximately in the same range. Models 21–24 are generated using the unsheared three bipole configuration and varying a from 0 to 1. As seen from Figure 5, a starts to become important only for values greater than 0.2 in Figure 5. These are unrealistically large, and we con-

clude, as expected, that plasma pressure and gravity forces have negligible effect in actual active regions.

3.3. General Scaling of the Magnetic Field versus Loop Length

Both the observed active regions and idealized theoretical models are well described by the function $F_1(L)$. The correlations are slightly better for the idealized models, as evidenced by the larger average correlation factors in Table 2. This can be attributed to two causes: magnetogram noise and large numbers of small flux concentrations that are present in the observed regions but not in the idealized models. Noise is treated as though it is real flux by the extrapolation procedure, and this gives rise to coronal field lines that should not exist. However, because noise has a spatial scale comparable to a pixel, it affects mainly the shortest extrapolated field lines and so it has a small effect on C_3 and S . We conclude that the difference is due to the larger number of flux concentrations in the observations than in the models. Finally, note that the correlation factors are larger for the $100 \leq B_f \leq 500$ G selection criterion, in part because noise is not a factor, and in part because the range of flux tubes is more restricted.

Another difference between the observed active regions and idealized models concerns the behavior of the fit parameter S in relation to S_{AR} . For the observed regions, S is systematically less than S_{AR} , varying from about half of S_{AR} in mature ARs to approximately S_{AR} in decaying ARs. This trend is especially evident for the $100 \leq B_f \leq 500$ G fits. In contrast, S and S_{AR} have the same average size in the idealized models, although they do not track each other closely. We can understand this difference by recognizing that S_{AR} only characterizes the dipolar aspects of the photospheric flux distribution. When the distribution is complex and has intermixed polarity centers, S_{AR} does not necessarily reflect the separation of these centers. For example, consider the extreme case of a region of fully mixed field, as in most of the quiet Sun during solar minimum. The value of S_{AR} for this region will be zero, even though the opposite polarity network elements have a characteristic separation scale. Since the observed active regions are more complex than the idealized models, we expect their S_{AR} values to be systematically lower in comparison to S .

The behaviors of C_2 and C_3 are quite similar for the observed active regions and idealized models. For both groups, $C_2 \approx 0$, indicating that field strength is statistically independent of length for field lines shorter than S . Also for both groups, C_3 increases from ≈ -3 in well-formed and simpler regions to ≈ -1 in the more complex configurations. The flaring regions have a higher coefficient C_3 than the quiet ones, on average. This is not surprising since

flares have always been associated with complex topologies (e.g., Démoulin et al. 1997). We conclude that the function F_1 accurately describes the statistical relationship between $\langle B \rangle$ and L over a wide range of field line lengths. The results for $\langle B^2 \rangle$ are similar, except that C_3 is more negative (the slope is steeper) by the amount -0.65 (see § 3.1).

4. A LAW FOR A RESTRICTED RANGE OF LOOP LENGTHS

The general law discussed above involves parameters that vary from one active region to the next (primarily S and C_3). It would be much more convenient to have a universal law with a single parameter or parameters that are the same for all cases. This is especially true if we wish to combine our results with those of Klimchuk & Porter (1995), which were obtained from a collection of loops observed in many different active regions. Let us consider the simplest case of a power law, $B \propto L^\delta$, as adopted by Klimchuk & Porter. We have already shown that $F_1(L)$ reduces to this form in the limits $L \ll S$ and $L \gg S$. Does a power law also apply over a limited range of intermediate lengths ($L \approx S$), where most of the coronal loops are observed? In this section we show that, indeed, it does and, furthermore, that the value of δ is similar for all active regions (i.e., it is universal)!

4.1. Observed Regions

The SXT loops included in the Klimchuk & Porter study have lengths in the range $[50, 300]$ Mm. As shown in Figure 3, this is also the approximate range of S , which is the location in L where the scatter plot distributions have their knee and change slope. Since the knee occurs at different L values for different regions, we expect that a composite distribution composed of all the scatter plot data combined would wash out the individual knees and produce a more linear dependence on L . We have verified that this is in fact the case. We therefore fit the individual active region distributions over limited length intervals to the function

$$F_2(L) = C + \delta \log L. \quad (13)$$

Note that this is equivalent to $B = 10^C L^\delta$ when $F_2 = \log B$. We consider the interval $[50, 300]$ Mm, corresponding to the observed SXT loops, as well as the modified intervals $[50, 400]$ and $[30, 300]$ Mm. Figure 6 shows δ as a function of the AR number (Table 1) for the case $B_f \geq 10$ G. Results for $100 \leq B_f \leq 500$ G are similar. In Table 4, we list the average values of δ and their standard deviations. We also give the average correlation factors indicating the quality of the fits. The most striking aspect of the results is that δ is confined to a rather narrow range. It depends only weakly on the precise interval of field line length. This provides

TABLE 4
AVERAGE VALUES OF THE SLOPES AND CORRELATION FACTORS TO F_2

B_f Range	$\delta(\langle B \rangle)$	$\delta(\langle B^2 \rangle)$	$r(\langle B \rangle)$	$r(\langle B^2 \rangle)$
Observed Regions				
$10 \leq B_f$	-0.84 ± 0.21	-1.28 ± 0.39	0.66 ± 0.13	0.56 ± 0.16
$100 \leq B_f \leq 500$ G	-1.11 ± 0.29	-1.82 ± 0.47	0.88 ± 0.05	0.87 ± 0.06
Models				
$10 \leq B_f$	-1.05 ± 0.17	-1.65 ± 0.39	0.64 ± 0.09	0.52 ± 0.09
$100 \leq B_f \leq 500$ G	-1.14 ± 0.25	-1.82 ± 0.42	0.93 ± 0.05	0.89 ± 0.09

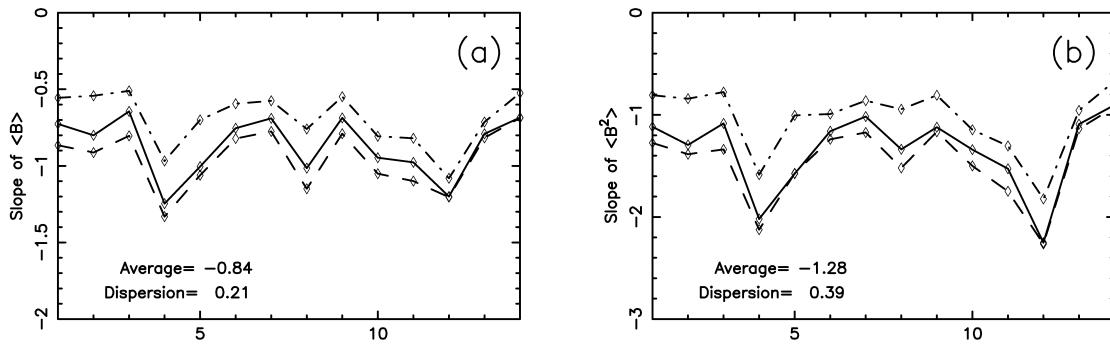


FIG. 6.—Results from fitting the linear function F_2 to the scatter plot data derived from the observed active regions (described in Table 1). The slope δ is plotted against the region number for (a) $\langle B \rangle$ and (b) $\langle B^2 \rangle$. The solid curve is for the range of loop lengths in the study of Porter & Klimchuk (1995, i.e., [50, 300] Mm). The upper (lower) curve is for a range of [30, 300] ([50, 400]). The selected field lines have B_f greater than 10 G.

further evidence that a universal scaling law exists for observed coronal loops.

4.2. Simplified Configurations

We have performed an identical analysis of the idealized theoretical models described in § 3.2. Results are presented in Figure 7 and Table 4. Again, δ lies within a narrow range, similar to that for the observed active regions. The reason for this behavior can be understood by analyzing the slope of F_1 , since δ is essentially the average slope of F_1 over a restricted interval of L . Taking $C_2 = 0$ to simplify the expression, we have

$$\frac{dF_1}{d \log L} = \frac{C_3 L^2}{S^2 + L^2}. \quad (14)$$

As can be seen from Figure 5 and to a lesser extent from Figure 3, there is a substantial tendency for C_3 and S to be anticorrelated. Thus, C_3 becomes more negative when S increases, and the changes tend to offset each other in equation (14). This explains why different active regions have comparable slopes even when their C_3 values and S values are dissimilar.

4.3. A Universal Power Law for Active Region Loops

We have shown that a power law of the form L^δ provides a good statistical fit for both $\langle B \rangle$ and $\langle B^2 \rangle$ in the range of L corresponding to observed coronal X-ray loops (approximately [50, 300] Mm). The value of δ exhibits no significant dependence on the age or complexity of the active region, or on whether the region is quiet and flaring. Only strong asymmetries in the areas of the leading and

following polarities ($A_s \geq 3$, which are rare) and large values of the average shear ($\alpha_s \geq 2 \times 10^{-2} \text{ Mm}^{-1}$) produce significant deviations in δ . We conclude that $\langle B \rangle$ and $\langle B^2 \rangle$ are related to L by a power law, as supposed by Klimchuk & Porter (1995), and that the slope of this power law has an almost “universal” value: -0.97 ± 0.25 for $\langle B \rangle$ and -1.55 ± 0.43 for $\langle B^2 \rangle$.

We can compare this with the recent results of Aschwanden et al. (1999), who analyzed 30 loops observed in a single active region by the Extreme Ultraviolet Imaging Telescope (EIT) and the Michelson Doppler Imager (MDI) experiments on the *Solar and Heliospheric Observatory* (SOHO). They measured the lengths of the loops using a “dynamic stereoscopy” technique and obtained a mean value of 433 Mm and a rather small standard deviation of 136 Mm. They then assigned footpoint field strengths to the loops by finding the strongest MDI magnetogram pixels in the vicinity of the observed ends. These values range mostly between 50 and 400 G. Finally, assuming a power-law dependence, they found a best-fit slope of -1.02 ± 0.43 , which is remarkably close to our value of -0.97 .

We can also compare our result to another more indirect estimation of δ . Using *Skylab* data, Golub et al. (1980) derived a statistical relationship of the form $P_{AR} \propto B_{AR}^b$ relating the average plasma pressure and average magnetic field strength of active regions of different size and emissivity. This approach is different from that of Klimchuk & Porter, who studied individual loops and deduced a relationship $P \propto L^\beta$. Nevertheless, the sizes of the Golub et al. active regions and the Klimchuk & Porter loops are comparable, and it is tempting to combine the two results to obtain $B \propto L^{\beta/b}$. This provides an observational estimate of $\delta = \beta/b$

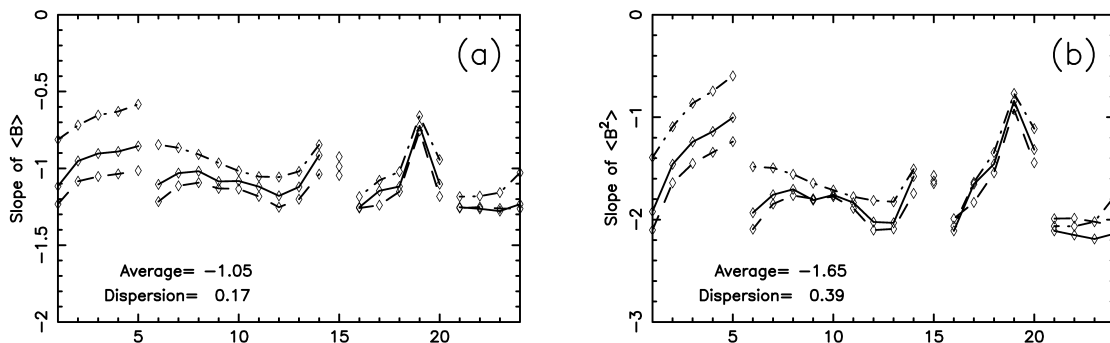


FIG. 7.—Same as Fig. 6 but for the idealized models described in Table 3

with an uncertainty

$$\Delta\delta = |\delta| [(\Delta\beta/\beta)^2 + (\Delta b/b)^2]^{1/2}. \quad (15)$$

Taking $b = 1.6$ as given by Golub et al. and $\beta = -0.96 \pm 0.8$ as given by Klimchuk & Porter, we find that $\delta_{\text{obs}} = -0.6 \pm 0.5$, where we have assumed a conservative value of ± 0.3 for Δb . This estimate for δ is higher (less negative) than the one we have deduced, but still within the error bars.

Sturrock & Uchida (1981) have noted that the results of Golub et al. are strongly biased by a single data point that was taken from a different study. Considering the possibility that this is inappropriate, they conclude that b could lie anywhere in the range $[0.6, 1.9]$! Adopting this range, we get $\delta'_{\text{obs}} = -0.77 \pm 0.8$. This estimate is closer to ours, although the uncertainty is substantial. We conclude that our results obtained directly from magnetic field extrapolations are consistent with those obtained more indirectly from the scaling of the plasma pressure with field strength in ARs.

5. CAN WE CONSTRAIN CORONAL HEATING MODELS?

5.1. An Overview on Coronal Heating Models

Models or theories of coronal heating can be divided into two main categories: stressing models, in which energy is extracted from coronal magnetic fields that are stressed by slow footpoint motions, and wave models, in which energy is deposited by waves that are incident from below. These

are also sometimes referred to as direct current (DC) and alternating current (AC) models, respectively. Many models address the question of how the free magnetic energy or wave energy is dissipated, while others are concerned only with the origin of this energy and do not prescribe a specific dissipation mechanism. We now describe briefly a number of different models, first considering those in the stressing category and then considering those in the wave category. The models are listed in Table 5 together with the scaling laws that they predict. The parameters included in these laws are defined either in this section or in § 5.2. We note that the parameter R that appears in many of the scaling laws cannot always be interpreted straightforwardly as the loop radius. We defer discussion of this and of the parameter τ until after the models are presented (see § 5.1.3).

5.1.1. Stressing Models

Photospheric and subphotospheric motions displace magnetic footpoints in both random and systematic ways and can include both translational and rotational components. The magnetic free energy that is pumped into the field can be released in real time or stored in the field to be released later. Thus, the resulting plasma heating can be steady, quasi-steady, or highly episodic, depending on the model. Quasi-steady heating refers to situations where the time interval between heating events is short compared to the cooling time by radiation and thermal conduction.

Stochastic buildup.—Model 1 (Sturrock & Uchida 1981; Berger 1991) considers the random twisting of individual

TABLE 5
SUMMARY OF THE SCALING LAW FOR DIFFERENT MODELS OF CORONAL HEATING

Model Characteristics	N^0	References	Scaling Law	Parameters
Stressing Models (DC)				
Stochastic buildup	1	1	$B^2 L^{-2} V^2 \tau$	
Critical angle	2	2	$B^2 L^{-1} V \tan \theta$	
Critical twist	3	3	$B^2 L^{-2} V R \phi$	
Reconnection $\propto v_A$	4	4	$BL^{-2} \rho^{1/2} V^2 R$	
Reconnection $\propto v_{A\perp}$	5	5	$B^{3/2} L^{-3/2} \rho^{1/4} V^{3/2} R^{1/2}$	
Current layers	6	6	$B^2 L^{-2} V^2 \tau \log R_m$	
	7	7	$B^2 L^{-2} V^2 \tau S^{0.1}$	
	8	8	$B^2 L^{-2} V^2 \tau$	
Current sheets	9	9	$B^2 L^{-1} R^{-1} V_{\text{ph}}^2 \tau$	
Taylor relaxation	10	10	$B^2 L^{-2} V_{\text{ph}}^2 \tau$	
Turbulence with:				
Constant dissipation coefficients	11	11	$B^{3/2} L^{-3/2} \rho^{1/4} V^{3/2} R^{1/2}$	
Closure	12	12	$B^{5/3} L^{-4/3} \rho^{1/6} V^{4/3} R^{1/3}$	
Closure + spectrum	13	13	$B^{s+1} L^{-1-s} \rho^{(1-s)/2} V^{2-s} R^s$	$s = 0.7, m = -1.$
	14			$s = 1.1, m = -2.5$
Wave Models (AC)				
Resonance	15	14	$B^{1+m} L^{-3-m} \rho^{-(1+m)/2}$	$m = -1.$
	16			$m = -2.$
Resonant absorption	17	15	$B^{1+m} L^{-1-m} \rho^{-(1+m)/2}$	$m = -1.$
	18			$m = -2.$
	19	16	$B^{1+m} L^{-m} \rho^{-(m-1)/2}$	$m = -1.$
	20			$m = -2.$
Current layers	21	17	$BL^{-1} \rho^{1/2} V^2$	
Turbulence	22	18	$B^{5/3} L^{-4/3} R^{1/3}$	

REFERENCES.—(1) Sturrock & Uchida 1981, Berger 1991; (2) Parker 1988, Berger 1993; (3) Galsgaard & Nordlund 1997; (4) Parker 1983; (5) Parker 1983, modified; (6) van Ballegoijen 1986; (7) Hendrix et al. 1996; (8) Galsgaard & Nordlund 1996; (9) Aly & Amari 1997; (10) Heyvaerts & Priest 1984, Browning & Priest 1986, Vekstein et al. 1993; (11) Einaudi et al. 1996, Dmitruk & Gómez 1997; (12) Heyvaerts & Priest 1992, Inverarity et al. 1995, Inverarity & Priest 1995a; (13) Milano et al. 1997; (14) Hollweg 1985; (15) Ofman et al. 1995, Ruderman et al. 1997; (16) Halberstadt & Goedbloed 1995; (17) Galsgaard & Nordlund 1996; (18) Inverarity & Priest 1995b.

flux tubes which produces a stochastic buildup of energy. Although the amount of twist may be increasing or decreasing at any given moment, there is a long-term increase due to the random nature of the process (random walk in twist angle). The energy grows linearly with time, on average, and is assumed to dissipate episodically at intervals that are long compared with the correlation time of the flow. The heating events can be large or small and can eliminate all or part of the twist. This scaling law also applies to stochastic energy buildup resulting from random translation motions, but the random walk step size must be short compared to the correlation length of the flow pattern so that field lines do not wrap around each other.

Critical angle.—When the random walk step size is not short compared to the correlation length, the field becomes entangled and braided, and the energy builds quadratically with time in a monotonic fashion. This is the scenario in model 2 (Parker 1988; Berger 1993), which supposes that heating occurs when a critical angle θ is reached between adjacent misaligned flux tubes. Parker suggests that a steady state is set up in which dissipation balances energy input to maintain the angle at or close to the critical value. In fact, the same scaling law applies even if the heating is highly episodic and the angle decreases substantially between events. We can extend the model to the case of flux tubes that are twisted rather than braided. The only change to the scaling law is that θ must now be interpreted as the angle between the twisted field lines at the outer edges of adjacent tubes.

Critical twist.—Model 3 (Galsgaard & Nordlund 1997) is similar, except that energy release occurs when a flux tube reaches a critical twist angle, ϕ , perhaps due to the onset of a kink instability. Note that ϕ is the end-to-end angular rotation of the twisted tube, which is different from θ .

Reconnection.—Magnetic reconnection may be responsible for the conversion of magnetic to thermal energy in the above models, but this is not explicitly treated. In model 4 (Parker 1983), it is the prescribed mechanism. It is assumed to occur at tangential discontinuities (current sheets) that are postulated to form even in simple magnetic configurations when footpoints are displaced by continuous motions. The scaling law is derived by equating the magnetic reconnection rate with the energy buildup rate. If we modify Parker's original derivation to account for the fact that the reconnection rate is likely to depend on the transverse field strength, rather than the total field strength, we obtain model 5, with a somewhat different scaling law.

Current layers.—There is considerable skepticism that current sheets will actually form from continuous footpoint motions unless the coronal magnetic field is sufficiently complex (contains nulls, separatrices, etc.). Nonetheless, there is widespread agreement that currents can easily become concentrated in layers of small but finite thickness. In model 6 (van Ballegooijen 1986), energy that is pumped into the field over large scales gradually cascades to smaller and smaller scales until eventually the scale is small enough for Ohmic dissipation to be effective. This is a purely kinematic cascade in the sense that the coronal field responds quasi-statically to the boundary motions. It is different from the dynamic cascades that occur in turbulence, as discussed later. Models 7 (Hendrix et al. 1996) and 8 (Galsgaard & Nordlund 1996) are fundamentally similar to model 6, except that they involve MHD simulations. Simple footpoint shearing motions are imposed at the boundary with

the direction of motion rotating by 90° at time intervals selected randomly. Currents develop exponentially at stagnation points in the corona, but they are dissipated rather suddenly after growing for only about one correlation time of the driver. No significant braiding occurs. A primary difference from model 2 (the critical angle model) concerns the energy buildup time between heating events. In models 7 and 8, this is roughly the flow correlation time, which is the same for all loops, but in model 2, the energy builds until the critical angle is reached, and this takes more time for long loops than for short ones.

Current sheets.—Model 9 (Aly & Amari 1997) considers the formation and destruction of true current sheets in magnetic configurations containing X-points. Such sheets appear and grow naturally from X-points in the presence of a steady flow (convergent flow in this model, but any flow in general). It is proposed that these sheets dissipate episodically, by magnetic reconnection, in a sequence of energy release events. For the scaling law in Table 5, we have accounted for the fact that most of the energy release will be confined to those field lines that have undergone reconnection.

Taylor relaxation.—Model 10 (Heyvaerts & Priest 1984; Browning & Priest 1986; Vekstein, Priest, & Steele 1993) makes use of Taylor's well-known conjecture (Taylor 1974) that magnetic fields relax via reconnection to the lowest energy state that conserves helicity—the linear force-free state. In this scenario, footpoint motions produce nonlinear force-free fields, and these fields episodically relax to the corresponding linear field having the same helicity, thereby releasing energy. The relaxation timescale, τ , enters into the scaling law in different ways depending on the specific assumptions that are made.

Turbulence.—It is well known that turbulence develops in ordinary fluids whenever the Reynolds number is larger than about 100 (e.g., Landau & Lifshitz 1959). Turbulence may also develop in the corona, where the Lundquist number exceeds the critical threshold by many orders of magnitude (although there is some question about the stabilizing influence of line tying). This has led a number of authors to propose coronal heating models in which the small spatial scales necessary for effective dissipation are produced by turbulence. As in model 6, energy is pumped into the field at large scales, and it cascades to smaller scales where the heating can more readily occur. Unlike model 6, the cascade is a dynamical effect resulting from the nonlinearities in the governing equations and is only weakly related to the details of the boundary motions.

Two different approaches have been used to study turbulent heating in the corona. Model 11 (Einaudi et al. 1996; Dmitruk & Gómez 1997) involves MHD simulations in a two-dimensional plane corresponding to a cross-sectional cut across a flux tube. Forcing terms are included in the equations to approximate the influence of adjacent planes, which are magnetically coupled to the plane of the calculation. The coefficients of resistivity and kinematic viscosity are constant and, for computational reasons, much larger than actual coronal values. Turbulence develops as part of the time-dependent solution and is not assumed a priori. Models 12 (Heyvaerts & Priest 1992; Inverarity, Priest, & Heyvaerts 1995; Inverarity & Priest 1995a) and 13 (Milano, Gómez, & Martens 1997) are fully three dimensional, but the nonlinear terms in the Equations are replaced by diffusion terms which mimic the effects of an assumed turbu-

lence. The turbulent diffusion coefficients are free parameters and are determined self-consistently according to “closure models” that relate the magnitudes of the coefficients to the magnitude of the energy cascade and, hence, the magnitude of the energy input by footpoint driver motions. These motions are assumed to have a Kolmogorov spectrum in wavenumber ($\propto k^{-5/3}$), and model 13 also includes a power-law spectrum in frequency ($\propto \omega^m$). The parameter s in the scaling law is related to m as indicated in the last column of Table 5.

5.1.2. Wave Models

Waves occur in coronal loops whenever the timescale of the motions is shorter than the end-to-end Alfvén travel time. Although waves can be generated directly in the corona, such as by bursty reconnection, we do not consider that situation here since the energy that powers the waves resides initially in the stressed coronal magnetic fields. We instead concentrate on models in which the waves are generated at the base of the corona, possibly by photospheric turbulence, and propagate upward to heat the corona.

Resonance.—Because of the steep density and temperature gradients at the footpoints of coronal loops, wave energy can be both reflected and transmitted at the boundary. The loop acts as a driven, leaky, resonance cavity. Model 15 (Hollweg 1985) addresses the conditions that must be met in order for significant energy to be transmitted into the loop from below. Similar sorts of conditions are satisfied by antireflective coatings on camera lenses. The scaling law for this model depends on the power-law index of the assumed driver frequency spectrum, m . Note that the constant of proportionality in this and other wave heating scaling laws is not dimensionless, and the complete form has the correct physical units.

Resonant absorption.—Models 17–20 (Ofman, Davila, & Steinolfson 1995; Ruderman et al. 1997; Halberstadt & Goedbloed 1995) consider a different aspect of loop resonance. Whenever the Alfvén velocity is nonuniform in a loop cross section—for example, if the density varies with radial distance away from the loop axis—a phenomenon known as resonant absorption occurs. The wave amplitude is enormously enhanced in a narrow layer where the local Alfvén resonance frequency matches the frequency of the global loop oscillations. Gradients in the magnetic field and velocity are extremely large in this layer, and the wave energy is easily dissipated by Ohmic and viscous processes. Note that Ofman, Davila, & Shimizu (1996) (as well as Klimchuk & Porter 1995) obtained a somewhat different scaling law than that of model 17 because they did not relate the global loop oscillations in the simulations, which have a nonflat energy spectrum, to the spectrum of the presumed external driver. This turns out to have little impact on the results presented in § 5.5.

Current layers.—Model 21 (Galsgaard & Nordlund 1996) is basically the same model as model 8 but taken in the limit of rapid boundary excitations compared to the end-to-end Alfvén travel time. Compared to previous wave models, one major difference is that the boundary condition is not described by a power-law spectrum in frequency, but rather by a series of shearing motions randomly modified. In this AC limit of the model the total dissipation in the loop is independent of its length.

Turbulence.—Model 22 (Inverarity & Priest 1995b) is similar to model 12 except that the footpoint motions have

a high enough frequency to produce waves rather than a quasi-static evolution. The loop cross section has a uniform Alfvén speed, so there is no resonant absorption. Instead, the waves are dissipated via a turbulent cascade to small scales.

5.1.3. The Meaning of Certain Parameters

The interpretation of the scaling laws in Table 5 is not always as simple as one would like. For example, the parameter R is in some instances just the loop radius. Any twisting motions then lead to a slightly different scaling law depending on whether the loop does [case (b)] or does not [case (a)] expand above the photosphere according to § 5.4. In other instances, R is a characteristic horizontal length scale for the magnetic field and/or flow field, and it can only be interpreted very loosely as a loop radius. For some models, especially those involving turbulence, the random driver motions produce an unknown combination of translation and twist, and the impact of flux tube lateral expansion is not obvious. We therefore italicize R only for those models where it is clear that case (a) and case (b) should be different; otherwise, we do not.

Another complication concerns the parameter L . For most models this is simply the loop length, but for models 9, 10, 12, and 22 it is the characteristic width of an assumed magnetic arcade. The scaling law applies to the spatially averaged heating rate throughout the arcade, even though the arcade is composed of many different flux tubes of differing length (for model 9, the heating will tend to be concentrated near the separatrix). The scaling laws should therefore be applied to observations of individual loops only with caution.

Several of the models involve a parameter τ . In some cases it represents the correlation time of the driver flow, and in other cases (models 9 and 10) it represents the characteristic time interval between heating events. Some models imply a weak dependence on the magnetic Reynolds number R_m or the Lundquist number S . We assume that τ , as well as θ , ϕ , R_m , and S , are independent of loop length, and we include them in Table 5 only for completeness. We remind the reader that the $H \propto L^{-2}$ scaling law of Klimchuk & Porter was determined under the assumption that the observed loops are heated quasi-steadily. This will not be the case if the time interval between heating events is long compared to the cooling time.

5.2. How Can Observations Test Heating Models?

The aim of coronal-heating models is to identify the mechanism responsible for the energy input at coronal heights. However, many of the hypotheses involved (e.g., the formation of small scale lengths) are not directly verifiable with present observations. One test that is typically applied to models is to compare the predicted heating rate with that obtained from observations. Several models pass this test successfully for both quiet Sun and active region conditions. The aim of our work is, finally, to provide more severe constraints by comparing the dependence given by models with those deduced from observations.

For simplicity, we consider the heating of individual coronal loops. In this paper we will use results obtained on X-ray loops, but the magnetic scaling laws obtained in §§ 3 and 4 can be used in a broader context. Coronal loops can refer to the bright structures that are easily distinguishable in soft X-ray and EUV images, or to the “diffuse” corona,

which can be thought of as a collection of tightly packed loops having similar properties (note that even the diffuse corona may be comprised of distinct structures that are below our resolution limit). As shown in Table 5, most coronal heating models give a heating rate per unit volume which can be expressed in the following generic way:

$$H_m \propto B^a L^b \rho^c V^d R^e, \quad (16)$$

where B and ρ are the coronal field strength and plasma density, L is the loop length, and V is the transverse velocity at the base of the corona, while the meaning of R has been discussed in § 5.1.3. The coronal base is located a small distance above the photosphere, at the height where the field has expanded out to become essentially force free, as discussed below. The coefficients a through e predicted by a variety of models are given in Table 5.

If B , ρ , V , and R have a known power-law dependence on L , equation (16) reduces to the simple form

$$H_m \propto L^{\alpha_m}, \quad (17)$$

where the subscript m indicates a model quantity. This can be compared to the observed relationship

$$H \propto L^{\alpha} \quad (18)$$

determined from *Yohkoh* data by Porter & Klimchuk (1995). If α_m and α agree to within the uncertainties, then the model can be considered viable. Otherwise, it must be rejected. Porter & Klimchuk obtained independent estimates of α based on the observed relationships $P \propto L^{\beta}$ and $T \propto L^{\gamma}$. The pressure scaling gives a most probable value for α of -1.95 with a 90% confidence interval of $[-3.11, -0.95]$, while the temperature scaling gives -2.00 and $[-4.59, -0.67]$. Note that the most probable values are essentially identical, and in § 5.5 we refer to a single result.

In this paper, we have shown how B scales with L . To proceed, we must know how the other physical variables in equation (16) scale with L . The density scaling can be inferred from the pressure and temperature results given by Porter & Klimchuk:

$$\rho \propto L^{\epsilon}, \quad (19)$$

where $\epsilon = \beta - \gamma = -0.96$. We have recently performed a direct statistical analysis of the density and length data for these same loops and find a nearly identical value of $\epsilon = -0.90$, where the 90% confidence interval is $[-1.55, 0.20]$. How V and R depend on loop length is much less certain, and we return to this issue in § 5.4.

5.3. Nonuniformity of the Magnetic Field

In the above discussion, we have glossed over the precise meaning of B in equation (16). The models we have summarized in Table 5 are based on a highly idealized corona. For example, most of them assume a quasi-uniform magnetic field between two plates that are meant to represent the positive and negative polarity parts of the photosphere. This fully neglects the magnetic complexity of observed configurations. In particular, with these restrictions, only a characteristic field strength (B) is present in the prediction of the heating rate (eq. [16]). What is the meaning of B in the context of magnetic extrapolation where the field strength is found to vary along every field line? We can define a heating averaged along the loop because parallel conduction efficiently transports energy along the loop. Then the heating is approximately proportional to $\langle B^a \rangle$ (a'

could be different from a in the case when V or R depend on B , as in eqs. [21] and [23]). Since for most models we have $1 \leq a' \leq 2$ we have chosen to use two limiting cases: $B = \langle B \rangle$ and $B = \langle B^2 \rangle^{1/2}$ as defined by equations (7) and (8). The results of § 4 show that the relationship $B(L)$ is only minimally sensitive to the average chosen. Therefore, the test of the models is not severely influenced by the details of how the field strength is averaged.

Furthermore, observations show that coronal loops have a nearly constant cross section (Klimchuk et al. 1992). Because the magnetic field is divergence free, this implies that the field strength should be nearly uniform along a coronal loop. The variation of the field strength obtained with our magnetic field extrapolations is then likely to be only an artifact of the potential approximation used. However, without a good understanding of the physical reasons for the observed constant cross sections, it is not possible to extrapolate the field more accurately. This is a natural future extension of the present work.

5.4. Effects of Boundary Conditions

For all but the wave heating models, the source of the energy that heats the corona is the continual stressing of the field by photospheric or subphotospheric flows. These flows perform work on the field, and the increased magnetic energy is ultimately liberated into the plasma via some process. The temporally and spatially averaged heating rate in a loop can therefore be equated with the Poynting flux coming through the footpoints, which is relatively easy to determine.

The quantities V and R in equation (16) refer to the base of the corona, which is separated from the photosphere by the chromosphere and transition region. On the other hand, the driver motions which displace the coronal magnetic field are associated with convection, or some other turbulent or organized flows that originate at or below the solar surface. How are V and R related in these two regions? One possibility, which we refer to as case (a), is that the coronal and photospheric quantities are identical:

$$R = R_{\text{ph}}, \quad V = V_{\text{ph}} [\text{case (a)}]. \quad (20)$$

This is the assumption made for nearly all published models.

A second possibility, case (b), takes into account the well-known fact that the photospheric field is strongly concentrated in thin flux tubes. Magnetic flux conservation implies

$$R \approx R_{\text{ph}} \sqrt{\frac{B_{\text{ph}}}{B}} [\text{case (b)}]. \quad (21)$$

Any braiding or shearing motions in the photosphere are transmitted to the bottom of corona with nearly the same amplitude. However, the velocity of twisting motions will be amplified due to the flux tube expansion (van Ballegoijen 1986). For a stationary twisting motion, conservation of angular velocity gives

$$\omega = \frac{V}{R} \approx \frac{V_{\text{ph}}}{R_{\text{ph}}}. \quad (22)$$

Then, using equation (21), the twisting velocity at the base of the corona is

$$V \approx V_{\text{ph}} \sqrt{\frac{B_{\text{ph}}}{B}} [\text{case (b)}]. \quad (23)$$

Because plasma densities are so much larger in the photosphere than in the corona, it is reasonable to suppose that photospheric quantities are essentially unaffected by the physical conditions of the corona. This suggests that B_{ph} , R_{ph} , and V_{ph} are statistically independent of the coronal loop length, L . With this hypothesis, the power-law index in equation (17) has the form α_m given by

$$\alpha_m = \delta a + b + \epsilon c \text{ for case (a) ,} \quad (24)$$

and

$$\alpha_m = \delta(a - (d + e)/2) + b + \epsilon c \text{ for case (b) ,} \quad (25)$$

where we have assumed that other parameters intrinsic to some of the models are also statistically independent of the loop length L . If the errors in δ and ϵ are uncorrelated, the uncertainty in the index is

$$\Delta\alpha_m = [a^2(\Delta\delta)^2 + c^2(\Delta\epsilon)^2]^{1/2} \text{ for case (a) ,} \quad (26)$$

and

$$\Delta\alpha_m = [(a - (d + e)/2)^2(\Delta\delta)^2 + c^2(\Delta\epsilon)^2]^{1/2} \text{ for case (b) .} \quad (27)$$

5.5. Test on the Heating Models

Figure 8 shows the values of α_m predicted by the different models in Table 5. Error bars are based on equations (26) and (27), where we use

$$\epsilon = -0.90, \Delta\epsilon = 0.88 . \quad (28)$$

For the magnetic field scaling, we use

$$\delta = -0.88 \pm 0.3 , \quad (29)$$

which is the average of δ obtained with $\langle B \rangle$ and $\delta/2$ obtained with $\langle B^2 \rangle$, for both ranges of B_f . Note that the conclusions we draw below are not affected by the precise choice of δ .

The horizontal line in Figure 8 indicates the observed value, α , determined by Porter & Klimchuk. The shaded bands indicate the 90% confidence intervals determined with the pressure scaling (*dark, narrow band*) and the tem-

perature scaling (*light, broad band*). Neither interval is centered on the most probable value. In order for a model to be strictly consistent with the *Yohkoh* observations, its error bar must overlap with the dark band. Only some of the models satisfy this requirement. However, in all but models 17–20, the disagreement is quite small, and given the approximate nature of the error estimations, it is not appropriate to reject these models as impossible.

We nonetheless find that some models are in better agreement with the observations than others. In particular, with the hypothesis of no flux expansion [case (a)], models in which energy release occurs at a critical angle of the magnetic field (Parker 1988; Berger 1993; model 2) or which involve magnetic reconnection (Parker 1983; models 4 and 5; Aly & Amari 1997; model 9) or which involve turbulence (Einaudi et al. 1996; Dmitruk & Gómez 1997; Heyvaerts & Priest 1992; Inverarity, Priest, & Heyvaerts 1995; Inverarity & Priest 1995a; models 11 and 12) predict α_m very close to the most probable value. Wave heating models, especially models 17–20, exhibit the poorest agreement with these observations with the remarkable exception of model 15 (Hollweg 1985) while models 21 and 22 (Galsgaard & Nordlund 1996; Inverarity & Priest 1995a) are both close to the most probable value of α . Taking into account the magnetic flux expansion [case (b)], nearly all the stressing models (except model 10, which involves Taylor relaxation) are closer to the most probable value determined by Porter & Klimchuk. This is a warning that flux-tube expansion should be treated in models (rather than the often used uniform field).

6. CONCLUSIONS

The main motivation of this work has been to provide observational constraints on coronal heating models by testing their predictions for the heating rate as a function of several physical parameters. Because thermal conduction transports energy efficiently along field lines, and not across them, coronal loops are the fundamental building blocks of the corona. For quiescent loops—which have lifetimes much longer than their cooling times—scaling laws relate statistically the temperature, pressure, heating rate, and length of the loops. Porter & Klimchuk (1995) applied these laws to *Yohkoh* observations to deduce how the heating rate

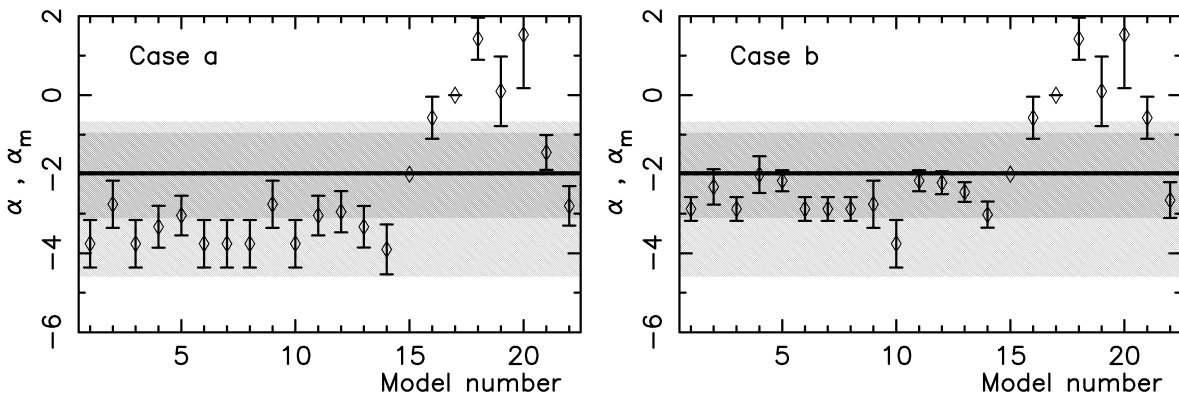


FIG. 8.—Comparison of the heating rate vs. length scaling law, $H \propto L^\alpha$, as deduced from observations and models. The plotted points with error bars indicate the power-law index α_m predicted by the models listed in Table 5. The horizontal line at $\alpha = -2$ is the most probable value deduced from observations (Porter & Klimchuk 1995), with the dark (light) shaded band representing the 90% confidence interval associated with the pressure (temperature) measurements.

scales with L . To use this result as a test of the models requires further information on how other basic parameters scale with L . The most important of these parameters is the coronal magnetic field strength, and so we have investigated its statistical relationship to loop length using extrapolations of the photospheric magnetic field.

We found that the averages $\langle B \rangle$ and $\langle B^2 \rangle$ along elemental flux tubes are both statistically well represented by a function $\propto (L^2 + S^2)^{C_3/2}$. Thus, the averages are nearly constant for $L < S$, and they follow a power law L^{C_3} for $L > S$. To within a factor of 2, the size scale S is linked to the characteristic size of the active region. The value of C_3 for $\langle B \rangle$ ranges typically between -3 and -1 . The lower limit corresponds to a simple bipole at large distances. Most active regions are far more complex than this, and C_3 becomes less negative as the complexity increases. The results for $\langle B^2 \rangle$ are similar, the main difference being that C_3 is typically more negative by the amount -0.65 .

In the range of loop lengths studied by Porter & Klimchuk (1995), [50, 300] Mm, we found that the general law reduces to a simple power law of the form L^δ . The index δ has a nearly constant value of -0.97 ± 0.25 for $\langle B \rangle$ and -1.55 ± 0.43 for $\langle B^2 \rangle$. In contrast to the general law, there is no systematic dependence on the maturity or complexity of the active region. We showed how this is due to the offsetting influences of S and C_3 .

We then used these results to test models of coronal heating by comparing the predicted scaling of heating rate with L to that determined observationally by Porter & Klimchuk (1995). We want to stress that the scaling law derived by these authors refers to long-lived loops, mostly in active regions. Ofman et al. (1996) found a different scaling law, $H \propto L^{0.6}$, for loop transient brightenings. The most striking aspect of Figure 8 is that the stressing models, as a group, are in much better agreement with observations than are the wave models. Most have error bars that either overlap or nearly overlap the dark gray band, which is the most stringent observational constraint from the study of Porter & Klimchuk (small differences are not significant due to the approximate nature of the error estimates). In contrast, many of the wave models have error bars lying well outside this band and must be considered untenable in their present form. Models 15, 21, and 22 are exceptions. The latter two have counterparts in the stressing category (models 8 and 12). The only real difference for these models is the frequency of the imposed driver motions (DC vs. AC motions). Moreover, they are the only wave models in Table 5 that have no power spectrum in frequency imposed at the boundary.

Comparisons of this kind have obvious value, but further observational and theoretical progress is necessary before we can identify the detailed mechanism of coronal heating with confidence. First, the observational value of α must be determined much more accurately. Broadband plasma diagnostic techniques such as those used by Porter & Klimchuk are not sufficiently precise for these purposes. We suggest that the best way to proceed is through spectroscopic measurements of loop temperature and density using instruments like the Solar Ultraviolet Measurements of Emitted Radiation (SUMER) and the Coronal Diagnostic Spectrometer (CDS) on board *SOHO*, or perhaps the new spectrometer that will fly on the upcoming *Solar-B* mission.

Second, the magnetic field properties of coronal loops must be better understood. We have here examined flux tubes without regard for whether they correspond to X-ray loops. This is a potential drawback, since the nearly constant thickness of observed loops suggests that their magnetic fields may be different from those in the surrounding fainter regions. Perhaps they are more highly twisted, as suggested by Klimchuk et al. (1992). A detailed understanding of the magnetic structure of individual loops must probably await the high spatial resolution vector field measurements from *THEMIS* and *Solar-B*.

Much progress is also required in the area of theory/modeling. Due to the inherent complexity of coronal physics, most of the existing models treat only one aspect of the complete coronal heating problem. For example, model 2 allows for multiple wrapping and braiding of the field, as one would expect from random footpoint motions, but it does not provide a detailed description of the dissipation mechanism. Conversely, models 7 and 8 treat the dissipation explicitly (if only approximately), but because of the unrealistically small Reynolds numbers that must be used, the dissipation sets in before any appreciable wrapping or braiding can occur. Wave models are similarly limited in their scope. Model 15 is spectacularly successful in matching the observations, but this is for a particular power-law spectrum in frequency ($\propto \omega^{-1}$), and it only treats the question of wave transmission. Its uniform corona does not allow for resonant absorption effects, which we know are important in actual nonuniform coronal loops. These effects are treated properly in models 17–20 (although see Ofman, Klimchuk, & Davila 1998), but those models ignore the important transmission effects. A complete model of wave heating is still lacking. Many of the turbulence models (11, 12, and 22) appear very promising. Unfortunately, they all assume a flat frequency spectrum, and a more realistic spectrum can change the results rather dramatically (models 13 and 14; Milano et al. 1997). Two important points, omitted in many models, are to take into account the expansion of flux tubes from the photosphere to the corona and to include boundary conditions closer to observed ones. In addition, work needs to be done to evaluate the possible influence that photospheric line tying has on the development of coronal turbulence. At the present time, we conclude that stressing models involving slow footpoint motions are more likely to be the correct explanation of coronal heating than are wave models, but a definitive statement must await further observational and theoretical progress.

We wish to thank Mona Hagyard, Jack Harvey, Axel Hofmann, and Jean Rayrole for providing us the magnetograms from Marshall, Kitt Peak, Potsdam, and Meudon, respectively. The American data used here are produced cooperatively by NSF/NAO, NASA/GSFC, and NOAA/SEL. We thank Giorgio Einaudi, Daniel Gómez, Joe Hollweg, Leon Ofman, Grigory Vekstein, and Marco Velli for helpful discussions on their models. P. D. and C. H. M. acknowledge financial support from ECOS (France) and SECYT (Argentina) through their cooperative science program (A97U01). The work of J. A. K. was supported by NASA contract W-19,200.

REFERENCES

- Acton, L. W. 1996, in *Magnetodynamic Phenomena in the Solar Atmosphere—Prototypes of Stellar Magnetic Activity*, ed. Y. Uchida, T. Kosugi, & H. Hudson (Dordrecht: Kluwer), 3
- Aly, J. J., & Amari, T. 1997, *A&A*, 319, 699
- Aschwanden, M. J., Newmark, J. S., Delaboudinière, J. P., Neupert, W. M., Klimchuk, J. A., Gary, G. A., Portier-Fozzani, F., & Zucker, A. 1999, *ApJ*, 515, 842
- Berger, M. A. 1991, *A&A*, 252, 369
- . 1993, *Phys. Rev. Lett.*, 70, 705
- Bray, R. J., Cram, L. E., Carrant, C. J., & Loughhead, R. E. 1991, *Plasma Loops in the Solar Corona* (Cambridge: Cambridge Univ. Press)
- Browning, P. K., & Priest, E. R. 1986, *A&A*, 159, 129
- Démoulin, P., Bagalá, L. G., Mandrini, C. H., Hénoux, J. C., & Rovira, M. G. 1997, *A&A*, 325, 305
- Dmitruk, P., & Gómez, D. O. 1997, *ApJ*, 484, L83
- Einaudi, G., Velli, M., Politano, H., & Pouquet, A. 1996, *ApJ*, 457, L113
- Falconer, D. A. 1997, *Sol. Phys.*, 176, 123
- Fisher, G. H., Longcope, D. W., Metcalf, T. R., & Pevtsov, A. A. 1998, *ApJ*, 508, 885
- Galsgaard, K., & Nordlund, A. 1996, *J. Geophys. Res.*, 101, 13445
- . 1997, *J. Geophys. Res.*, 102, 219
- Golub, L., Maxson, C., Rosner, R., Serio, S., & Vaiana, G. S. 1980, *ApJ*, 238, 343
- Grotian, W. 1939, *Naturwissenschaften*, 27, 214
- Halberstadt, G., & Goedbloed, J. P. 1995, *A&A*, 301, 559
- Hagyard, M. J., Cumings, N. P., West, E. A., & Smith, J. E. Jr. 1982, *Sol. Phys.*, 80, 33
- Hendrix, D. L., Van Hoven, G., Mikić, Z., & Schnack, D. D. 1996, *ApJ*, 470, 1192
- Heyvaerts, J., & Priest, E. R. 1984, *A&A*, 137, 63
- . 1992, *ApJ*, 390, 297
- Hollweg, J. V. 1985, in *Adv. in Space Plasma Physics*, ed. B. Buti (Singapore: World Scientific), 77
- Inverarity, G. W., & Priest, E. R. 1995a, *A&A*, 296, 395
- . 1995b, *A&A*, 302, 567
- Inverarity, G. W., Priest, E. R., & Heyvaerts, J. 1995, *A&A*, 293, 913
- Kano, R., & Tsuneta, S. 1996, *PASJ*, 48, 535
- Klimchuk, J. A. 1990, *ApJ*, 354, 745
- Klimchuk, J. A., Lemen, J. R., Feldman, U., Tsuneta, S., & Uchida, Y. 1992, *PASJ*, 44, L181
- Klimchuk, J. A., & Porter, L. J. 1995, *Nature*, 377, 131
- Landau, L. D., & Lifshitz, E. M. 1959, *Fluid Mechanics* (Oxford: Pergamon)
- Livingston, W. C., Harvey, J., Slaughter, C., & Trumbo, D. 1976, *Appl. Opt.*, 15, 40
- Low, B. C. 1992, *ApJ*, 399, 300
- Mandrini, C. H., Démoulin, P., van Driel-Gesztelyi, L., Schmieder, B., Cauzzi, G., & Hofmann, A. 1996, *Sol. Phys.*, 168, 115
- Metcalf, T. R., Canfield, R. C., Hudson, H. S., Mickey, D. L., Wülser, J. P., Martens, P. C. H., & Tsuneta, S. 1994, *ApJ*, 428, 860
- Mickey, D. L. 1985, *Sol. Phys.*, 97, 223
- Milano, L. J., Gómez, D. O., & Martens, P. C. H. 1997, *ApJ*, 490, 442
- Ofman, L., Davila, J. M., & Shimizu, T. 1996, *ApJ*, 459, L39
- Ofman, L., Davila, J. M., & Steinolfson, R. S. 1995, *ApJ*, 444, 471
- Ofman, L., Klimchuk, J. A., & Davila, J. M. 1998, *ApJ*, 493, 474
- Orrall, F. Q. 1981, *Solar Active Regions* (Boulder: Colorado Associated Univ. Press)
- Parker, E. N. 1983, *ApJ*, 264, 642
- . 1988, *ApJ*, 330, 474
- Pevtsov, A. A., Canfield, R. C., & McClymont, A. N. 1997, *ApJ*, 481, 973
- Porter, L. J., & Klimchuk, J. A. 1995, *ApJ*, 454, 499
- Priest, E. R., Foley, C. R., Heyvaerts, J., Arber, T. D., Culhane, J. L., & Acton, L. W. 1998, *Nature*, 393, 545
- Rayrole, J. 1980, *Proc. Japan-France Seminar on Solar Physics*, ed. J. C. Hénoux & F. Moriyama (Tokyo Astronomical Obs.), 258, 41
- Ruderman, M. S., Berghmans, D., Goossens, M., & Poedts, S. 1997, *A&A*, 320, 305
- Rust, D. M., & Kumar, A. 1996, *ApJ*, 464, 199
- Sams III, B. J., Golub, L., & Weiss, N. O. 1992, *ApJ*, 399, 313
- Schmieder, B., Démoulin, P., Aulanier, G., & Golub, L. 1996, *ApJ*, 467, 881
- Staudé, J., Hofmann, A., & Bachmann, G. 1991, in *Solar Polarimetry*, ed. L. J. November (National Solar Obs., Sunspot), 49
- Sturrock, P. A., & Uchida, Y. 1981, *ApJ*, 246, 331
- Sturrock, P. A., Wheatland, M. S., & Acton, L. W. 1996, *ApJ*, 461, L115
- Taylor, J. B. 1974, *Phys. Rev. Lett.*, 33, 1139
- van Ballegoijen, A. A. 1986, *ApJ*, 311, 1001
- Vekstein, G. E., Priest, E. R., & Steele, C. D. C. 1993, *ApJ*, 417, 781